Carbon 174 (2021) 430–438

Contents lists available at ScienceDirect

Carbon

journal homepage: www.elsevier.com/locate/carbon

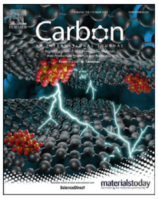

Converting plastic waste pyrolysis ash into flash graphene

Kevin M. Wyss [a], Jacob L. Beckham [a], Weiyin Chen [a], Duy Xuan Luong [a], Prabhas Hundi [d], Shivaranjan Raghuraman [b], Rouzbeh Shahsavari [b, **], James M. Tour [a, c, e, *]

[a] Department of Chemistry, 6100 Main ST MS 60, Houston, TX, 77005, USA
[b] C-Crete Technologies, 13000, Murphy Road, Unit 102, Stafford, TX, USA
[c] Smalley-Curl Institute, The NanoCarbon Center and the Welch Institute for Advanced Materials, Rice University, 6100, Main Street, Houston, TX, USA
[d] Department of Civil and Environmental Engineering, Rice University, TX, 77005, USA
[e] Department of Materials Science and NanoEngineering, Rice University, 6100, Main Street, Houston, TX, USA

ARTICLE INFO

Article history:
Received 26 October 2020
Received in revised form
16 December 2020
Accepted 20 December 2020
Available online 23 December 2020

Keywords:
Upcycle
Plastic waste
Pyrolysis ash
Flash joule heating
Turbostratic flash graphene

ABSTRACT

Pyrolysis of plastic waste (PW), a commercial method of recycling, is currently economically challenging and produces up to 20% by mass valueless pyrolysis ash (PA) as a byproduct. Here, direct, facile upcycling of PW-derived PA into high purity turbostratic flash graphene (tFG) is demonstrated. The tFG displays excellent dispersibility, yielding a concentration of 2.84 mg/mL in aqueous surfactant solution. The tFG was used to fabricate tFG-PVA nanocomposites, and low doses of tFG (0.1%–1%) improve failure strain by 15%–30% when compared to the samples of neat PVA. Further, the addition of tFG to PVA films showed decreased hydrophilic interactions, increasing the water contact angle by 235% and adsorbing 500% less water than neat PVA. The tFG was also added to Portland cement paste as well as concrete, and exhibited 43% and 25% increases in compressive strength, respectively. The tFG is used directly in both composite applications, requiring no purification or chemical functionalization, unlike many other products used in nanocomposites.

1. Introduction

Pyrolysis is a form of chemical recycling that leads to homolysis of plastic waste (PW) polymers in order to extract energy-rich gases, fuel oils, waxes, naphtha, and virgin monomers [1–3]. A byproduct of this PW beneficiation process (“beneficiation” is a treatment that increases the value of a feedstock by removing a low value waste stream) that can reach up to 20 wt% is carbon-rich pyrolysis ash (PA) that currently has low or negative value [4]. Chemical recycling is a promising method toward the formation of a circular plastic economy, but it may not be economically viable without political or commercial incentives and it struggles to compete with less expensive virgin oil and commodity monomers [5,6]. Through the upcycling of negative value byproducts to high value products, a circular plastics economy and decreased use of virgin chemical feedstocks might be achieved.

Graphene is a 2D material that has interesting mechanical, chemical, thermal, and electrical properties [7–11]. The use of graphene in composite materials shows particular promise since graphene-containing nanocomposites generally show significantly enhanced mechanical, electrical, and thermal properties [12,13]. Over the past decade, bulk graphene synthesis has involved a top-down method of converting graphite to graphene through physical or chemical exfoliation [14], or reduction of graphene oxide, which itself comes from graphite [15]. These synthetic methods are expensive, resource intensive, difficult to scale and yield varying qualities of graphene or graphene nanoplatelets [16]. Recently, we reported a scalable, bottom-up, low-cost synthesis of flash graphene (FG) [17]. The technique uses flash Joule heating (FJH) to heat carbonaceous materials to temperatures over 3000 K in ~100 ms, producing >90% yields of high quality turbostratic FG (tFG). The high temperatures of FJH result in high purity tFG, since much of the non-carbon atoms are removed through sublimation. Here, we use PA to produce tFG, then demonstrate the use of PA derived tFG for enhancement of poly(vinyl alcohol) (PVA) composites as well as Portland cement composites.

---

* Corresponding author. Department of Chemistry, Rice University, 6100 Main ST MS 222, Houston, TX 77005, USA.
** Corresponding author. C-Crete Technologies, 13000 Murphy Road, Unit 102, Stafford, TX, USA
E-mail addresses: rouzbeh@ccretetech.com (R. Shahsavari), tour@rice.edu (J.M. Tour).

https://doi.org/10.1016/j.carbon.2020.12.063
0008-6223/

2. Methods and methods

2.1. Chemicals and materials

PA was graciously provided by Shangqiu Zhongming Eco-Friendly Equipment Co., Ltd in Shangqiu City, Henan, China. PA was ground using a mortar and pestle before use. PVA (80% hydrolyzed, 9000–10,000 M_w) was obtained from Sigma-Aldrich and used without further purification or characterization. Pluronic-F127, a non-ionic surfactant, was obtained from Millipore-Sigma. Commercial graphene samples used for comparison were obtained from Tianyuan Empire Materials & Technologies, Shatin, Hong Kong and used without further purification.

2.2. Synthesis of FG

A custom made FJH station was built for the conversion of PA into FG as previously reported [17]. A circuit schematic and further details are shown in Figure S1. A capacitance of 60 mF was used to provide the current to the sample. PA (0.4 g) was compressed in a quartz tube and sandwiched between copper wool and copper electrodes to conduct current from the capacitors to the sample that had an initial resistance of ~15 Ω. The loaded quartz tube was enclosed in a vacuum desiccator to assist with sublimation of impurities, and the FJH apparatus was used to apply pulses of 50 V, 70 V, 90 V, and 160 V that each lasted 450 ms (total time 1800 ms) until a final resistance of 1 Ω resulted. After the FJH, the newly formed tFG was removed from the quartz tube, ground with a mortar and pestle, and used without further purification or treatment. Yields of 85–90 wt% were typically observed.

2.3. Fabrication of PVA and tFG-PVA samples

For the control sample, a bath ultrasonicated (30 min) solution of Pluronic-F127 in deionized water (200 mL of 1 wt%) was heated to 85 °C, at which point PVA (15 g) was added portion wise, and the mixture was stirred vigorously for 3 h. The solution was then reduced to a volume of 100 mL *via* rotary evaporation, and the viscous solution was poured into 3D printed polyvinyl butadiene (PVB) ASTM D412-A compliant dog bone molds for tensile strength testing or plastic petri dishes for contact angle and water adsorption measurements. Samples were then dried in an oven at 45 °C for 3 days.

For tFG or PA PVA-composite samples, a similar procedure was used except for the addition of the FG or PA to the 1 wt% Pluronic-F127 solution, followed by bath ultrasonication for 30 min at 25 °C. Then the Pluronic-F127 water solution containing tFG or PA was heated and PVA was added as detailed above.

2.4. Fabrication of tFG-OPC paste and tFG-OPC concrete samples

Ordinary Portland cement nanocomposites were prepared by dissolving varying concentrations of prepared tFG in a 1% water-Pluronic F-127 solution. The tFG was then dispersed *via* agitation for 15 min at 5000 rpm using a shear mixer (Silverson L5MA). The tFG dispersions were then mixed with Portland cement (0.40 water:cement ratio). The resulting slurry was then cast in 5 × 5 × 5 cm^3cubic PTFE molds, and allowed to solidify for 24 h, followed by curing in DI water for another 24 h. The compressive mechanical strength was tested after and additional 7 and 28 days of curing for OPC paste and OPC concrete, respectively.

2.5. Characterization and measurements

2.5.1. Raman spectroscopy

All Raman spectra of tFG were collected from samples ground by mortar and pestle and not exposed to solvent. Raman spectra of PVA films were carried out on samples with no further modification. At least ten randomly selected Raman spectra were collected for each sample and averaged to give a better representation. A Renishaw inVia Raman microscope outfitted with a 5 mW 532 nm laser was used, with 50× and 5× optical objective lenses to collect high magnification and low magnification spectra, respectively. The 50× optical objective lens was used to collect Raman maps.

2.5.2. X-ray diffraction

All XRD spectra were collected of samples ground by mortar and pestle and not exposed to solvent. A Rigaku D/Max Ultima II Powder XRD 6s were used to collect XRD patterns. A scan width of 0.05°/step and scan rate of 0.5°/min was used from 3° to 90°. Zero background sample holders were used.

2.5.3. Thermogravimetric analysis and differential scanning calorimetry

TGA thermograms were collected of samples ground by mortar and pestle and not exposed to solvent. A Q-600 Simultaneous TGA/DSC from TA Instruments was used. Alumina pans were used at a heating rate of 10 °C/min up to 780 °C. Atmospheric air at a flow rate of 80 mL/min was used to continuously purge the sample chamber unless otherwise noted.

2.5.4. Fourier transform infrared microscopy

All FT-IR spectra were collected on a Nicolet iN10 FTIR Infrared Microscope using the ATR attachment. PVA and composite film samples were analyzed immediately after drying; FG and PA samples were ground by mortar and pestle and not exposed to solvent before being analyzed by FT-IR.

2.5.5. UV–vis absorption spectroscopy

To determine the concentration of tFG present in dispersed aqueous solutions, varying amounts of finely ground tFG were added to a 1 wt% Pluronic-F127 aqueous solution. The solutions were bath ultrasonicated for 30 min at 25 °C, then centrifuged at 1000 g for 30 min. The supernatant was then diluted 200× and the absorbance measured at 660 nm. An extinction coefficient of 6600 l/g*m was used. A similar procedure was used to make PA dispersion UV–Vis analysis samples.

2.5.6. Tensile strength and modulus testing of tFG-PVA nanocomposites

PVA and PVA composite samples were prepared as detailed above, using an ASTM D412-A compliant dog bone mold and dried to constant mass. All mechanical tests were carried out in triplicate. The PVA and PVA composite samples were tested using an Instron 4505 Universal Testing Machine with a 100-kN static load cell and displacement boundary conditions were applied until failure. The load capacity of the grips is 100 kN and the spring stiffness of the testing device far exceeds the stiffness of the samples. Wedge grips were used to hold the samples firmly and apply tensile load uniformly over the entire cross section. In the tensile test a displacement rate of 1.27 mm min^{-1} was used.

2.5.7. Water uptake measurements

PVA and PVA composite samples were prepared as detailed above and dried to constant mass. Samples were then stored in a desiccator held at 100% relative humidity and maintained at 25 °C.

2.5.8. Scanning electron microscopy

SEM images were taken with a FEI Helios Nanolab 660 Dual Beam SEM System. To obtain images of isolated sheets, flakes of PA-derived tFG were sandwiched between two Si wafers coated with ~15 nm Au and exfoliated *via* the monodirectional application of shear force. Cross-sectional images of nanocomposites were obtained by slicing PVA and tFG-PVA composites laterally and imaging the opened surface. Low-voltage (1 keV) scans were taken of the PVA composites to minimize charging, while a voltage of 10 keV was employed in imaging the exfoliated FG flakes.

2.5.9. X-ray photoelectron spectroscopy

XPS data were collected with a PHI Quantera SXM Scanning X-ray Microprobe with a base pressure of 5×10^{-9} Torr. Survey spectra were recorded using 0.5 eV step sizes with a pass energy of 140 eV. Elemental spectra were recorded using 0.1 eV step sizes with a pass energy of 26 eV. All of the XPS spectra were corrected using the C 1s peaks (284.8 eV) as reference.

2.5.10. tFG-OPC Mechanical Strength Testing

Samples of tFG-OPC paste and tFG-OPC concrete were prepared as specified above, and tested in triplicate using a Forney Variable Frequency Drive automatic machine equipped with dual load cells to afford maximum accuracy.

2.5.11. Transmission electron microscopy

TEM images were collected using a JEOL 2100F TEM system using samples of tFG sonicated in ethanol, then drop cast on lacy carbon grids and allowed to air dry. An accelerating voltage of 200 kV was used.

2.5.12. Atomic force microscopy

AFM images were collected using a Park NX20 AFM system in non-contact mode. Samples of tFG and commercial graphene were prepared through sonication in ethanol, followed by drop casting on freshly cleaved mica.

3. Results and discussion

3.1. Synthesis and characterization of FG

tFG was synthesized from PA that resulted from the industrial pyrolysis of polypropylene PW at 450 °C. As part of the FJH process, the pulse voltage, duration, and initial sample resistance all impact the internal temperature reached and therefore control the sheet size, thickness, elemental purity, and defect concentration of the tFG. Hence, optimization of these parameters is essential to produce high-quality tFG.

Low-quality graphene typically exhibits a large D peak at 1350 cm^{-1}, signifying high disorder [18] resulting from defects in the sp [2]-hybridization of the graphene sheets and non-zigzag edges [19]. Small, broad 2D peaks at 2960 cm^{-1} signify the presence of multiple layer graphene with considerable interlayer electronic coupling [20] arising from the stacking of layers. When multilayer graphene is present, the 2D peak cannot be fitted with a single Lorentzian function since multiple phonon levels are present [21]. tFG is kinetically trapped, presumably because the millisecond time scale reaction does not allow for arrangement and stacking of the FG sheets in the thermodynamically favored Bernal AB-stacked form. Therefore, tFG is fit to a single Lorentzian [22]. Additionally, tFG should possess turbostratic TS_1 and TS_2 peaks (1875 cm^{-1} and 2025 cm^{-1}, respectively) as these peaks are positive indicators for turbostratic layer stacking. Finally, in tFG graphene there should be no M band present at ~1750 cm^{-1}. This M band has been attributed to the overtone of out-of-plane transverse optical phonon [21]. In tFG, the layers are incommensurate and there is no interlayer confinement in the adjacent layers; hence, the M band is not present.

While high magnification Raman spectroscopy provides a wealth of information on the interlayer dynamics in graphene, powder x-ray diffraction (XRD) and thermogravimetric analysis (TGA) allow for complimentary characterization of the bulk properties of the tFG produced. As shown in Fig. 1, use of a pulse voltage of 160 V and a pulse duration of 450 ms provides the optimal 2D/G ratio, the smallest D peak, and the least residual PA by powder XRD analysis. A pulse time of 450 ms was chosen since it allowed the sharpest 2D peak *via* Raman spectroscopy, and the best full width half maximum (FWHM) to be achieved for the (002) peak in the powder XRD at 26.1°. The (100) face of graphene is shown by the presence of the peak at 42.5°. A flash voltage of 160 V was chosen since it produced the best 2D/G ratio as well as the sublimation of heteroatoms without increasing the power consumption. A graph of current discharge over time, collected through use of a Hall effect sensor, can be seen in Figure S2.

The thermal stability of the tFG was directly correlated to the degree of conversion of PA to tFG. At longer durations and higher voltages approaching the optimized parameters, the thermal stability improved significantly (**Fig. 2**). The PA starting material contained ~10 wt% non-carbon contaminants and fillers that did not degrade *via* TGA even at 800 °C, but they persist and become oxidized. Analysis of the FG indicated that inorganic contaminants and fillers were sublimed from the sample since complete degradation of the tFG is observed in the TGA by 800 °C. TGA indicates that there is no residual PA since no weight loss is observed below 550 °C in the optimized tFG samples. After FJH, a mass yield of 85–90% is generally achieved, meaning that >90% of the carbon present in the PA is upcycled to tFG, a harbinger for the favorable prospects of this approach being used in large scale.

X-Ray photoelectron spectroscopy (XPS) was carried out to determine the degree of purification afforded by the FJH process (Figure S3). As shown in Table 1, the starting material contained significant oxygen content as well as sulfur and zinc. These heteroatoms are not detected by XPS after the optimized FJH process, therefore <0.2% based on XPS limits of detection of heavier elements in a light element matrix. High resolution XPS data of the carbon peak for both the raw PA and the produced tFG were collected (Figure S4). The initial PA shows significant oxygen content, in the form of C—O—C or C—OH bonds, with the rest of the carbon taking an sp [3]-hybridization. In the produced tFG, the most dominant bonding state is sp [2]-hybridization, and a greatly reduced *C*—O presence. No C=O is detected during the FJH process.

For composite applications, the production of tFG is helpful since the non-AB-stacked arrangement facilitates dispersion of tFG into composites, resulting in the need for lower loadings. A Raman spectrum of the tFG produced from PA is shown in Fig. 3, indicating that it turbostratic. The fitting of a single Lorentzian indicates it is electronically decoupled from other turbostratically stacked sheets. The presence of the TS_1 and TS_2 peaks and the absence of a clear M peak at ~1750 cm^{-1} indicates the uncoupled, non-AB stacked nature of the tFG [23,24].

The sheet size and morphology of graphene used in the material composite impacts the chemical, mechanical, and electrical behavior. To study the morphology of PA-derived tFG, high-resolution scanning electron microscopy (SEM) images were taken. Previously completed studies of the morphology of carbon black-derived FG reports two characteristic morphologies; a fine black powder referred to as “wrinkled graphene” that morphologically resembles non-graphitizing carbon but possesses the Raman signature of graphene; and larger gray crystals, found to be tFG [25]. Similar morphologies were observed in FG derived from

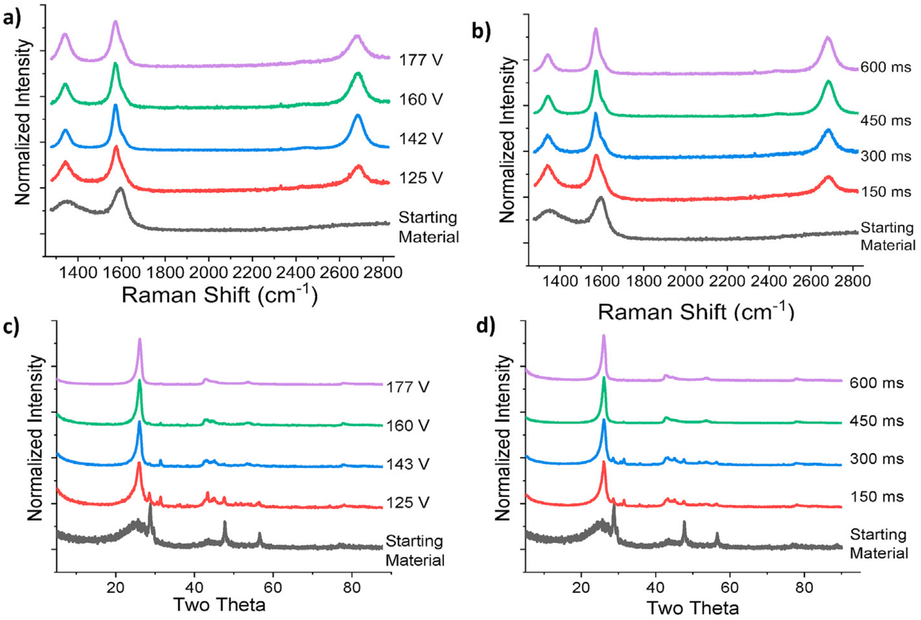

Fig. 1. Optimization of a) pulse voltage at 450 ms as analyzed by Raman spectroscopy (538 nm excitation), b) pulse duration at 160 V as analyzed by Raman spectroscopy (538 nm excitation), c) pulse voltage for 450 ms as analyzed by powder XRD, and d) pulse duration at 160 V as determined by powder XRD. All spectra shown are representative of the entire product as analyzed over 15 spots. (A colour version of this figure can be viewed online.)

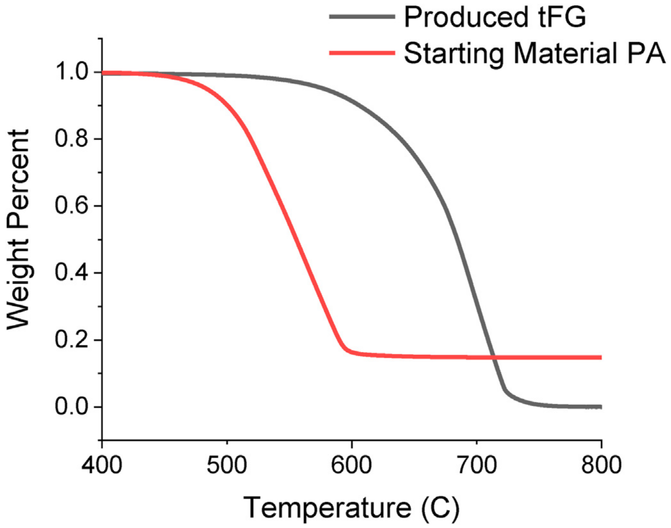

Fig. 2. TGA showing the thermal stability of tFG under atmospheric conditions with an air flow rate of 80 mL/min, using a ramp rate of 15 °C/min. (A colour version of this figure can be viewed online.)

Table 1
The elemental composition of PA and tFG as determined by XPS.

XPS element peak	PA	tFG Product
C 1s	88.52%	97.26%
O 1s	8.95%	2.74%
S 2p	1.55%	0.00%
Zn 2p3	0.98%	0.00%

PA and were separated using a 250 μm sieve for SEM study. Fig. 4a–c shows representative images of the wrinkled graphene and large tFG crystals, respectively. The gray crystals could be easily exfoliated by shear. FJH induces the formation of nanocrystalline domains of mobile carbon, similar to those shown in Fig. 4b. As heating time increases through prolonging pulse duration in the FJH (~500 ms), these crystals assemble into larger sheets, such as those shown in Fig. 4c. Fig. 4d–f shows FG sheets sheared onto a Si wafer that has been coated with Au to improve SEM contrast. The sheet size varies widely between the hundreds of nanometers and several microns. These large sheets might yield an enormous aspect ratio when exfoliated to single atom thicknesses *via* a surfactant, which strongly influences the resulting nanocomposite properties.

A total of 20 batches produced 5 g of tFG in <4 h. The electrical cost is previously calculated to be <$100/ton, and industrial implementation is also being studied [17]. The quality of the tFG was confirmed by averaging 45 randomly selected Raman spectra (Figure S5), showing an average 2D/G ratio of 0.83 and an average D/G ratio of 0.37. Powder XRD and TGA were used to confirm the quality of the 5 g batch of tFG (Figures S6 and S7). Powder XRD of the optimized material showed a pronounced (002) peak with a maximum located at 25.96°. Using Braggs law, and a CuKα value of 1.5418 Å, this corresponds to an interlayer spacing of 3.522 Å. This is significantly increased from the 3.34 Å that occurs in bulk AB-stacked graphite. The increased interlayer spacing results from the decreased π- π stacking interactions, which are disrupted by the rotational disorder that occurs in turbostratic graphene. This weakening of π-π stacking interactions, resulting in easier exfoliation of bulk tFG into 1–3 layer thick sheets, as shown by AFM (Figure S8). The interlayer spacing and sheet size was further studied using transmission electron microscopy (TEM), shown in Fig. 5. Here an interlayer spacing of 0.349 nm can be observed, with sheet sizes ranging from ~20 nm to multiple microns, with high degrees of turbostratic crystallinity being displayed.

The tFG was dispersed in a 1% aqueous surfactant solution to examine its colloidal stability in composite synthesis applications. As shown in Fig. 6, *in situ* concentrations of tFG reach 2.8 mg/mL after sonication and centrifugation. To ensure that the dispersed material was indeed tFG and eliminate the possibility that the dispersed material was PA (control dispersions are shown in Figure S9), the solution was drop cast onto a silica substrate and

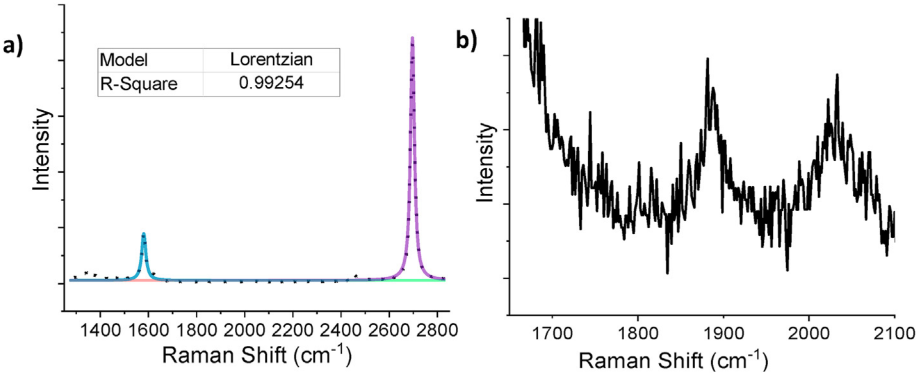

Fig. 3. a) Lorentzian fitting of the Raman spectrum from an exemplary area of the sample (actual spectrum dashed line, Lorentzian fit solid line); b) presence of TS$_1$ and TS$_2$ peaks and absence of M peak in the same spectrum. (A colour version of this figure can be viewed online.)

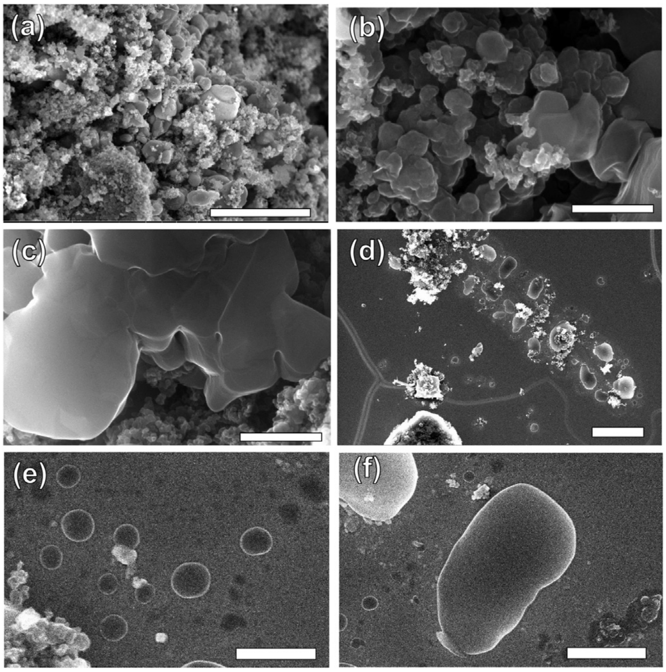

Fig. 4. SEM images of a) wrinkled graphene and (b–c) tFG crystals. Scale bars are 3 μm, 500 nm, and 500 nm, respectively. d) SEM image showing the exfoliation of tFG sheets onto an Au coated wafer. Scale bar 5 μm. e) Smaller exfoliated FG flakes of size ~200–300 nm. Scale bar 500 nm. f) A large tFG platelet. Scale bar 1 μm. (A colour version of this figure can be viewed online.)

examined by Raman spectroscopy. A 250 μm × 175 μm area was mapped (Figure S10), consisting of over 576 individual spectra, with the lowest 2D/G ratio observed being 0.65. The average spectrum is shown in Fig. 6b. No amorphous carbon was observed in the drop cast sample, indicating that little to no PA is present in the tFG dispersions. Due to concerns that the surfactant might artificially be affecting the dispersibility of tFG in solution, dispersibility in dimethylformamide (DMF) was also studied. In DMF, a stable dispersion of tFG of 0.79 mg/mL was achieved at a loading concentration of 7 mg/mL through use of bath sonication followed by centrifugation (Figure S11). We compared the dispersibility of the tFG to the dispersibility of commercially available graphene. At the same loading concentrations, the tFG was an average of 60 times more dispersible than commercial graphene. Due to the low oxygen content in tFG, solubility in pure aqueous solution is low, hence the necessary inclusion of surfactant. However, in surfactant assisted aqueous or DMF solution, commercial graphene is shown by AFM to aggregate whereas tFG does far less (Figure S8).

4. Characterization of tFG nanocomposite

PVA was chosen as the example composite system since it is a biodegradable, non-toxic, and biocompatible polymer [26] that is being extensively researched for medical applications, fuel cell polymer electrolyte membranes, and environmentally friendly packaging material [27]. However, PVA has not seen widespread use for consumer applications because of its poor mechanical properties, water solubility, and hydrophilicity.

Addition of graphene to synthesize polymer nanocomposites is often accomplished by melt-blending. Solution phase addition of tFG to the PVA was theorized to produce superior homogeneity at milder temperatures. Varying concentrations of tFG were added to form tFG-PVA composites of 0.1, 0.25, 0.5, 1.0 and 3.0 wt% tFG (Fig. 7). Similarly, varying concentrations of PA were added to PVA to act as control samples. That tFG lends superior exfoliation and dispersive properties can be readily seen with the naked eye when compared to amorphous carbon samples (Fig. 7a). The tFG-PVA nanocomposites were characterized with FT-IR and film Raman spectroscopy techniques (Fig. 7b–c) as well as film XRD (Figure S12), showing the strong presence of tFG. Commonly, chemical functionalization, partial ozone oxidation, or large amounts of copolymer are required to introduce graphene sheets homogeneously into the hydrophilic PVA solution [27]. This is unnecessary when using tFG since sample homogeneity is shown by both optical microscopy and SEM as well as Raman mapping (Figure S13 and S14).

The mechanical properties of the tFG-PVA nanocomposites were examined through tensile strength testing. Dog bone-shaped samples of neat PVA, PA-PVA, and nanocomposites of PVA with 0.1%, 0.25%, 1% and 3% tFG were tested for Young's modulus, tensile strength, failure strain and toughness. The results, as shown in Fig. 8 and Figure S15, indicate that compared to neat PVA, addition of PA leads to a reduction in modulus, strength and toughness. However, addition of tFG increases these properties. Tensile strength and Young's Modulus show a steady increase with addition of tFG and reach values similar to neat PVA. Failure strain, and as a result, toughness, show significant improvement through addition of low doses of tFG (0.1% ~ 1%). When the dose of tFG is increase to 3%, however, the failure strain decreased significantly. This can be attributed to the tendency of tFG to form aggregates at higher loading concentrations, leading to inconsistent distribution and formation of weak spots in the sample. Fig. 8b show stress-strain curves obtained during tensile testing of representative

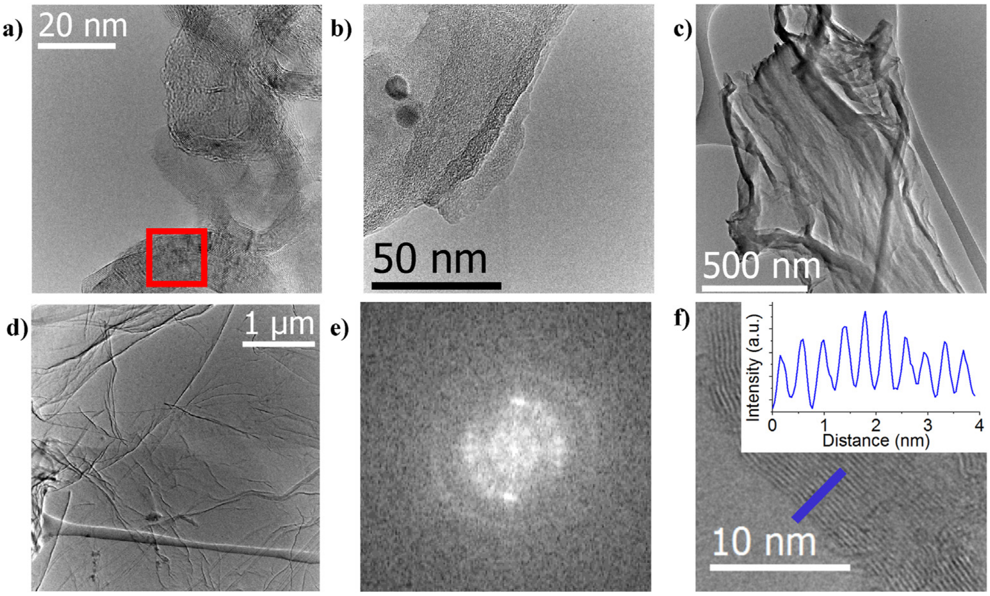

Fig. 5. a-d) TEM images of synthesized tFG; e) a Fourier transform of the highlighted region in 5a; f) a line scan intensity profile displaying the interlayer spacing present. (A colour version of this figure can be viewed online.)

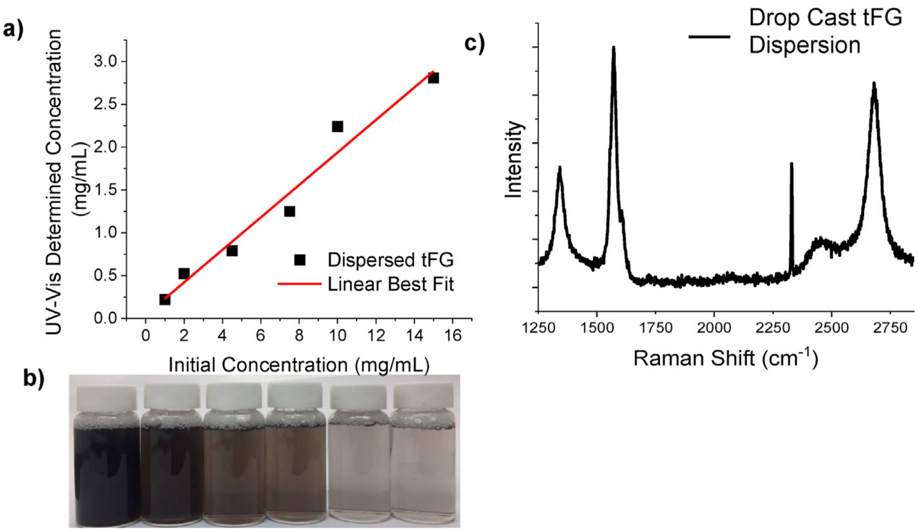

Fig. 6. a) UV–Vis absorption data at 660 nm used to determine the concentration of tFG present in solution as a function of amount loaded in sample. b) Photo of dispersions showing a 300× dilution of the tFG dispersions (concentrations pre-dilution L–R: 15, 10, 7.5, 4.5, 2, and 1 mg/mL). c) Raman spectrum of tFG dispersion solution drop-cast on silicon, showing the average spectra from 576 individual scans. The feature at ~2300 cm^{-1} results from a defect in the diffraction grating of the instrument, and is present when longer exposure times are used. (A colour version of this figure can be viewed online.)

samples that belong to each type. It is clearly observed that addition of low doses of tFG (0.1% ~ 1%) improves failure strain by 15%–30% when compared to the samples with neat PVA or PA-PVA composite.

Throughout literature, graphene is seen to significantly enhance the tensile strength of PVA composites, a phenomenon not observed here [28]. Traditional graphene/PVA nanocomposites are often formed through *in situ* reduction of GO to rGO, which has significant residual oxygen functionality content [29]. The extremely low oxygen content of tFG seemingly significantly impacts the composite properties of the tFG/PVA nanocomposites. In GO/PVA nanocomposites, strong inter-material hydrogen bonding results in high levels of dispersion, but these interactions disrupt the crystallinity, which results in lower enhancements in mechanical strength and modulus [30]. Often, the mechanism for modulus increase upon addition of graphene (rGO or pristine graphene) to PVA is attributed to significant increases in the crystallinity of PVA, coupled with the still present hydrogen bonding interactions [31]. The increase in crystallinity of PVA is actually a result of slight aggregation and orientation of pristine graphene restricts molecular movement and reptation of the PVA chains [32,33]. These findings taken together show that hydrogen bonding, facilitating strong inter-material junctions, and few-layer alignment of graphene sheets, facilitating higher degrees of crystallinity in the PVA matrix, are both necessary to produce significant increases in modulus. To this end, our findings that tFG does not significantly improve the tensile strength of PVA despite being well dispersed, is logical. Due to the low oxygen content in tFG

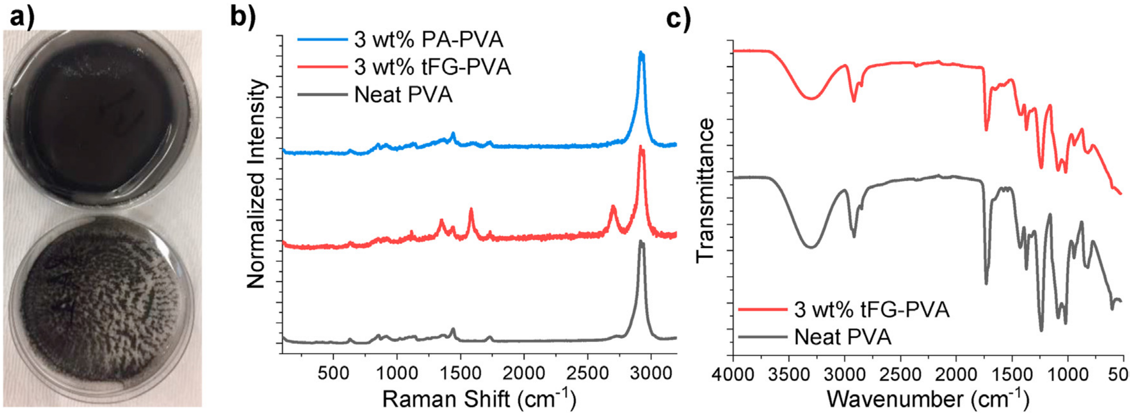

Fig. 7. a) Photo comparing a 0.1 wt% tFG-PVA composite (top) and 0.1 wt% amorphous carbon PA-PVA composite (bottom); b) Raman spectra of PVA composite samples; c) FT-IR spectra of neat PVA and PVA composite samples. (A colour version of this figure can be viewed online.)

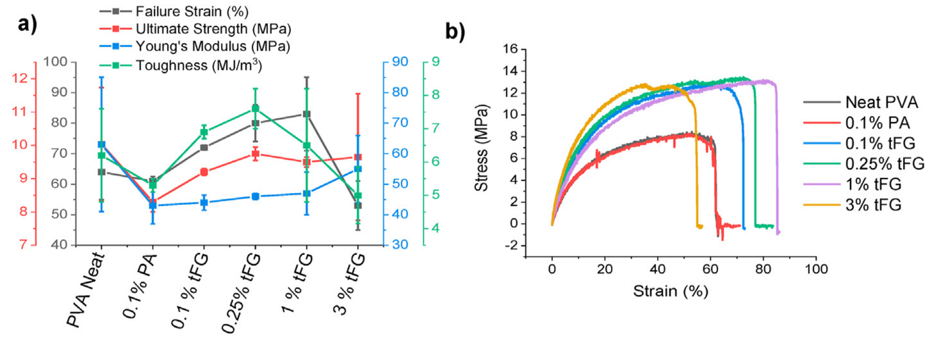

Fig. 8. a) Mechanical properties of PVA composites compared with neat PVA; b) stress-strain curves of representative PVA and PVA composite samples obtained from tensile tests. (A colour version of this figure can be viewed online.)

hydrogen bonding with the PVA is limited, and due to the turbostratic nature the few-layer alignment is also limited, which results in no significant increase in crystallinity in the PVA matrix.

Water permeability and degradation due to environmental humidity is a major hurdle in the implementation of PVA as a consumer packaging material. The hydrophobic properties of tFG resulted in significant decreases in water uptake, as well as resulting in a significant increase in contact angle when compared with neat PVA (Fig. 9). Decreasing the surface wettability, as shown by contact angle goniometry, shows a mitigation of the hydrophilic interactions of PVA and water by the high loading content of tFG. The samples are shown to be relatively homogenous by the small deviations in contact angles between trials. Also of note is that the glass transition temperature of the tFG-PVA nanocomposites increases slightly (from 48.4 to 50.6) as the tFG loading is increased (Figure S16). This observation sheds light on the interface between the PVA polymer chains and the tFG surfaces, showing that the lack of oxygen content in the graphene sheets results in minimal hydrogen bonding and polar interactions between the PVA matrix and nanocomposite additive. A smaller increase and also broadening in glass transition temperature was observed for 3% PA-PVA, which is likely due to aggregation of PA within the PVA matrix. These values for glass transition temperature are consistent with literature; however, more significant shifts in the Tg are generally

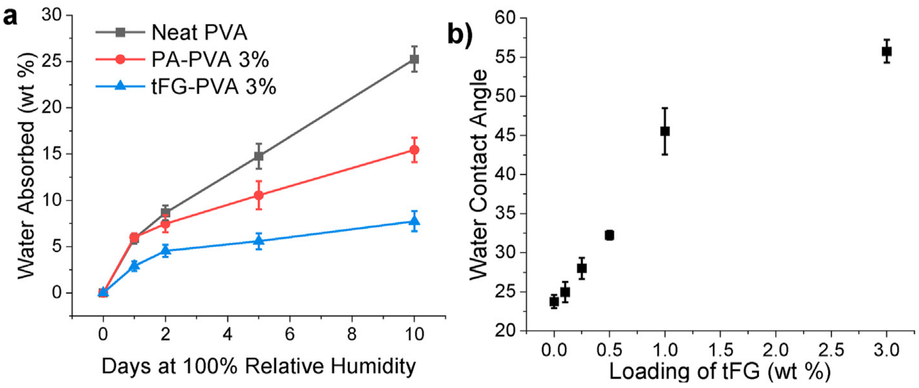

Fig. 9. a) Water uptake of tFG-PVA nanocomposites; b) water contact angle measurements of tFG-PVA nanocomposites. (A colour version of this figure can be viewed online.)

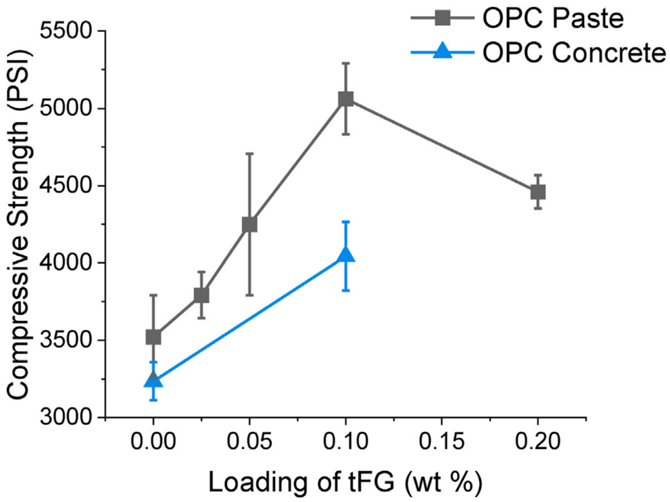

Fig. 10. Mechanical properties of tFG-OPC paste and tFG-OPC concrete nanocomposites, as compared to neat OPC paste and OPC concrete. (A colour version of this figure can be viewed online.)

observed at the graphene loading concentrations we observed [34–36]. These findings confirm the hypothesized lack of interaction between the tFG and PVA in the film environment.

To demonstrate another nanocomposite application of tFG, small amounts were added to ordinary Portland cement (OPC), and cured for 7 days and 28 days to yield tFG-OPC paste and tFG-OPC concrete respectively (Fig. 10). Significant increases in compressive strength were observed in both cases, with strength increasing as content of tFG increases in OPC paste, reaching an optimal loading at 0.1%. Compressive strength enhancement of 43% was observed for 0.1% enhanced OPC paste, and a 25% increase was observed for OPC concrete. This again underscores the utility of bulk production of graphene, and highlights the impressive mechanical properties of tFG nanocomposites.

5. Conclusion

A method to convert PW PA into tFG is reported. The tFG was used to enhance the mechanical and physical properties of PVA, needing no further functionalization or purification. A 50% increase in failure strain, as well as a 500% decrease in water uptake was observed, compared to neat PVA. The results demonstrate an environmentally friendly path for the reduction of PW by economically incentivized chemical recycling through the upcycling of PA to high value tFG, as well as the enhancement of polymers through addition of tFG to expand their implementation and range of applications.

CRediT authorship contribution statement

Kevin M. Wyss: Conceptualization, Investigation, Data curation, Writing - original draft, Writing - review & editing. **Jacob L. Beckham:** Investigation, Writing - original draft. **Weiyin Chen:** Investigation. **Duy Xuan Luong:** Investigation. **Prabhas Hundi:** Investigation. **Shivaranjan Raghuraman:** Investigation. **Rouzbeh Shahsavari:** Writing - original draft, Supervision, Writing - review & editing. **James M. Tour:** Conceptualization, Writing - original draft, Supervision, Writing - review & editing, Project administration, Funding acquisition.

Declaration of competing interest

The authors declare the following financial interests/personal relationships which may be considered as potential competing interests: Universal Matter Inc. has licensed from Rice University the FJH approach to graphene. J.M.T. is a stockholder in Universal Matter, but not an employee, officer or director. Potential conflicts of interest are mitigated through regular disclosures to and compliance with Rice University's Office of Sponsored Programs and Research Compliance. C-Crete Technologies owns intellectual property on the strengthening of graphene–cement/concrete composites.

Acknowledgement

K.M.W. and J.L.B. acknowledge the National Science Foundation Graduate Research Fellowship Program for graciously providing financial support. The Air Force Office of Scientific Research (FA9550-19-1-0296) and the DOE-NETL (DE-FE0031794) funded this work. Dr Bo Chen assisted with XPS analysis.

Appendix A. Supplementary data

Supplementary data to this article can be found online at https://doi.org/10.1016/j.carbon.2020.12.063.

References

[1] S.D. Anuar Sharuddin, F. Abnisa, W.M.A. Wan Daud, M.K. Aroua, A review on pyrolysis of plastic wastes, Energy Convers. Manag. 115 (2016) 308–326.
[2] R. Miandad, M.A. Barakat, A.S. Aburiazaiza, M. Rehan, A.S. Nizami, Catalytic pyrolysis of plastic waste: a review, Process Saf. Environ. Protect. 102 (2016) 822–838.
[3] S.M. Al-Salem, A. Antelava, A. Constantinou, G. Manos, A. Dutta, A review on thermal and catalytic pyrolysis of plastic solid waste (PSW), J. Environ. Manag. 197 (2017) 177–198.
[4] E. Menya, P.W. Olupot, H. Storz, M. Lubwama, Y. Kiros, M.J. John, Optimization of pyrolysis conditions for char production from Rice husks and its characterization as a precursor for production of activated carbon, Biomass Conv. Bioref. 10 (2020) 57–72.
[5] A. Fivga, I. Dimitriou, Pyrolysis of plastic waste for production of heavy fuel substitute: a techno-economic assessment, Energy 149 (2018) 865–874.
[6] J.M. Garcia, M.L. Robertson, The future of plastics recycling, Science 358 (2017) 870–872.
[7] K.S. Novoselov, A.K. Geim, S.V. Morozov, D. Jiang, Y. Zhang, S.V. Dubonos, I.V. Grigorieva, A.A. Firsov, Electric field effect in atomically thin carbon films, Science 306 (2004) 666–669.
[8] C. Lee, X. Wei, J.W. Kysar, J. Hone, Measurement of the elastic properties and intrinsic strength of monolayer graphene, Science 321 (2008) 385–388.
[9] X. Xu, L.F.C. Pereira, Y. Wang, J. Wu, K. Zhang, X. Zhao, S. Bae, C. Tinh Bui, R. Xie, J.T.L. Thong, B.H. Hong, K.P. Loh, D. Donadio, B. Li, B. Özyilmaz, Length-dependent thermal conductivity in suspended single-layer graphene, Nat. Commun. 5 (2014) 1–6.
[10] B.D. Briggs, B. Nagabhirava, G. Rao, R. Geer, H. Gao, Y. Xu, B. Yu, Electromechanical robustness of monolayer graphene with extreme bending, Appl. Phys. Lett. 97 (2010) 223102.
[11] J.-H. Chen, C. Jang, S. Xiao, M. Ishigami, M.S. Fuhrer, Intrinsic and extrinsic performance limits of graphene devices on SiO_2, Nat. Nanotechnol. 3 (2008) 206–209.
[12] R.J. Young, I.A. Kinloch, L. Gong, K.S. Novoselov, The mechanics of graphene nanocomposites: a review, Compos. Sci. Technol. 72 (2012) 1459–1476.
[13] V. Dhand, K.Y. Rhee, H. Ju Kim, D. Ho Jung, A comprehensive review of graphene nanocomposites: Research status and trends, J. Nanomater. 23 (2013) 14.
[14] Y. Xu, H. Cao, Y. Xue, B. Li, W. Cai, Liquid-phase exfoliation of graphene: an overview on exfoliation media, techniques, and challenges, Nanomaterials 8 (2018) 942.
[15] L. Dong, J. Yang, M. Chhowalla, K.P. Loh, Synthesis and reduction of large sized graphene oxide sheets, Chem. Soc. Rev. 46 (2017) 7306–7316.
[16] A.P. Kauling, A.T. Seefeldt, D.P. Pisoni, R.C. Pradeep, R. Bentini, R.V.B. Oliveira, K.S. Novoselov, A.H.C. Neto, The worldwide graphene flake production, Adv. Mater. 30 (2018) 1803784.
[17] D.X. Luong, K.V. Bets, W.A. Algozeeb, M.G. Stanford, C. Kittrell, W. Chen, R.V. Salvatierra, M. Ren, E.A. McHugh, P.A. Advincula, Z. Wang, M. Bhatt, H. Guo, V. Mancevski, R. Shahsavari, B.I. Yakobson, J.M. Tour, Gram-scale bottom-up flash graphene synthesis, Nature 577 (2020) 647–651.

[18] L.M. Malard, M.A. Pimenta, G. Dresselhaus, M.S. Dresselhaus, Raman spectroscopy in graphene, Phys. Rep. 473 (2009) 51–87.
[19] C. Casiraghi, A. Hartschuh, H. Qian, S. Piscanec, C. Georgi, A. Fasoli, K.S. Novoselov, D.M. Basko, A.C. Ferrari, Raman spectroscopy of graphene edges, Nano Lett. 9 (2009) 1433–1441.
[20] S. Shallcross, S. Sharma, E. Kandelaki, O.A. Pankratov, Electronic structure of turbostratic graphene, Phys. Rev. B 81 (2010) 165105.
[21] N. Gupta, S. Walia, U. Mogera, G.U. Kulkarni, Twist-dependent Raman and electron diffraction correlations in twisted multilayer graphene, J. Phys. Chem. Lett. 11 (2020) 2797–2803.
[22] P. Poncharal, A. Ayari, T. Michel, J.-L. Sauvajol, Raman spectra of misoriented bilayer graphene, Phys. Rev. B 78 (2008) 113407.
[23] J.-B. Wu, M.-L. Lin, X. Cong, H.-N. Liu, P.-H. Tan, Raman spectroscopy of graphene-based materials and its applications in related devices, Chem. Soc. Rev. 47 (2018) 1822–1873.
[24] J.A. Garlow, L.K. Barrett, L. Wu, K. Kisslinger, Y. Zhu, J.F. Pulecio, Large-area growth of turbostratic graphene on Ni(111) via physical vapor deposition, Sci. Rep. 6 (2016) 19804.
[25] M.G. Stanford, K.V. Bets, D.X. Luong, P.A. Advincula, W. Chen, J.T. Li, Z. Wang, E.A. McHugh, W.A. Algozeeb, B.I. Yakobson, J.M. Tour, Flash graphene morphologies, ACS Nano 14 (2020) 13691–13699.
[26] N.B. Halima, Poly(Vinyl alcohol): review of its promising applications and insights into biodegradation, RSC Adv. 6 (2016) 39823–39832.
[27] Z.W. Abdullah, Y. Dong, I.J. Davies, S.P.V.A. Barbhuiya, PVA blends, and their nanocomposites for biodegradable packaging application, Polym. Plast. Technol. Eng. 56 (2017) 1307–1344.
[28] S.K.S. Basha, K.V. Kumar, G.S. Sundari, M.C. Rao, Structural and electrical properties of graphene oxide-doped PVA/PVP blend nanocomposite polymer films, Ann. Mater. Sci. Eng. 2018 (2018) 4372365.
[29] C. Bao, Y. Guo, L. Song, Y. Hu, Poly(Vinyl alcohol) nanocomposites based on graphene and graphite oxide: a comparative investigation of property and mechanism, J. Mater. Chem. 21 (2011) 13942–13950.
[30] M. Cobos, M.J. Fernández, M.D. Fernández, Graphene based poly(vinyl alcohol) nanocomposites prepared by in situ green reduction of graphene oxide by ascorbic acid: influence of graphene content and glycerol plasticizer on properties, Nanomaterials (Basel) 8 (2018).
[31] R. Jan, A. Habib, M.A. Akram, T.-H. Zia, A.N. Khan, Uniaxial drawing of graphene-PVA nanocomposites: improvement in mechanical characteristics via strain-induced exfoliation of graphene, Nanoscale Res. Lett. 11 (2016) 377.
[32] Z. Li, R.J. Young, N.R. Wilson, I.A. Kinloch, C. Vallés, Z. Li, Effect of the orientation of graphene-based nanoplatelets upon the Young's modulus of nanocomposites, Compos. Sci. Technol. 123 (2016) 125–133.
[33] X. Yang, L. Li, S. Shang, X. Tao, Synthesis and characterization of layer-aligned poly(vinyl alcohol)/graphene nanocomposites, Polymer 51 (2010) 3431–3435.
[34] S. Cui, L. Li, Q. Wang, Enhancing glass transition temperature and mechanical properties of poly (propylene carbonate) by intermacromolecular complexation with poly (vinyl alcohol), Compos. Sci. Technol. 127 (2016) 177–184.
[35] Q. Bai, G. Zhang, B. Xu, X. Feng, H. Jiang, H. Li, Thermal and water dual-responsive shape memory poly(vinyl alcohol)/Al2O3 nanocomposite, RSC Adv. 5 (111) (2015) 91213–91217.
[36] T. Siddaiah, P. Ojha, N.O.G.V.R. Kumar, C. Ramu, T. Siddaiah, P. Ojha, N.O.G.V.R. Kumar, C. Ramu, Structural, optical and thermal characterizations of PVA/MAA:EA polyblend films, Mater. Res. 21 (5) (2018).